Nanoscale

PAPER

View Article Online
View Journal | View Issue

Cite this: *Nanoscale*, 2020, **12**, 6121

Stabilization of negative capacitance in ferroelectric capacitors with and without a metal interlayer†

T. Rollo, *[a] F. Blanchini, [b] G. Giordano, [c] R. Specogna [a] and D. Esseni *[a]

Received 6th November 2019,
Accepted 29th January 2020

DOI: 10.1039/c9nr09470a

rsc.li/nanoscale

The negative capacitance operation of a ferroelectric material is not only an intriguing materials science topic, but also a property with important technological applications in nanoscale electronic devices. Despite growing interest for possible applications, the very existence of negative capacitance is still actively debated, even because experimental results for ferroelectric capacitors with or without a metal interlayer led to quite contradicting indications. Here we present a comprehensive analysis of NC operation in ferroelectric capacitors and provide new insights into the discrepancies observed in experiments. Our models duly account for the three-dimensional nature of the problem and show a good agreement with several aspects of recent experiments. Our results also demonstrate that traps at the ferroelectric–dielectric interface play an important role in the feasibility of stable negative capacitance operation in ferroelectric capacitors.

1. Introduction

The basic idea behind the use of ferroelectric materials in nanoscale transistors stems from the fact that, thanks to the negative capacitance (NC) operation, the voltage swing necessary to operate the transistors can be reduced,[1–3] thus enabling improved energy efficiency for CMOS circuits.[4,5] An industrial level demonstration of NC operation in CMOS transistors was recently reported for a 14 nm FinFET technology,[6] with an analysis of the device and circuit level advantages further discussed in ref. 7. Moreover, several papers have started addressing diverse design aspects related to NC field effect transistors.[8–10]

Despite some encouraging experimental results, however, stable NC operation of ferroelectrics is still quite controversial.[11] In fact, recent studies in Metal–Ferroelectric–Insulator–Metal (MFIM) capacitors reported a hysteresis free, direct measurement of the negative capacitance branch of a thin ferroelectric layer.[12,13] However, in similar recent publications focused on Metal–Ferroelectric–Metal–Insulator–Metal (MFMIM) systems or on ferroelectric capacitors externally connected to a MOSFET authors either negated any evidence of NC operation,[14] or affirmed that the measured steep slope transistor operation was due to domain switching and, as such, invariably accompanied by hysteresis.[15–17]

The discrepancy between experiments in MFIM and MFMIM systems is not entirely unexpected; in fact a recent theoretical investigation suggests that MFMIM capacitors are inherently more prone than MFIM systems to domain nucleation.[18] The analysis in ref. 18, however, was restricted to a one-dimensional, rigidly periodic system and, moreover, conclusions were drawn by inspecting the free energy landscapes, instead of examining the actual ferroelectric dynamic equations of the MFIM and MFMIM systems.

In this paper we present a comprehensive analysis of the dynamics and possible stabilisation of a ferroelectric layer inserted either in a MFIM or in a MFMIM structure, which is a broadly extended version of the concise contribution reported in ref. 19. To this purpose we have developed a model for the depolarisation energy that fully accounts for the three-dimensional nature of the electrostatics in a realistic device. Then we use the multi-domain Landau–Ginzburg–Devonshire theory (LGD) and derive analytical or quasi-analytical conditions for stable NC operation, that explain the different behavior of a MFIM compared to a MFMIM capacitor. Our models are validated by good agreement with several aspects of recent experiments.[12,13] Finally we investigate the influence of possible traps at the ferroelectric–dielectric interface, and argue that traps not only help explain some experimental features,

[a] *DPIA, University of Udine, Via delle Scienze 206, 33100 Udine, Italy. E-mail: david.esseni@uniud.it*
[b] *DMIF, University of Udine, Via delle Scienze 206, 33100 Udine, Italy*
[c] *DII, University of Trento, via Sommarive 9, 38123 Povo, TN, Italy*

† Electronic supplementary information (ESI) available. See DOI: 10.1039/C9NR09470A

but also discriminate between a quasi-static and a dynamic NC operation.

2. Free energy and dynamic equations

In the analysis of the ferroelectric capacitors shown in Fig. 1 we assume that the spontaneous polarisation P lies along the z direction, and we write the free energy per unit volume of the ferroelectric as follows[18]

$$u_{\mathrm{F}} = \alpha P^2 + \beta P^4 + \gamma P^6 + k|\mathrm{grad}\, P|^2 + \frac{\varepsilon_0 \varepsilon_{\mathrm{F}}}{2} E_{\mathrm{F}}{}^2 \qquad (1)$$

where α, β and γ are the ferroelectric anisotropy constants, ε_0 is the vacuum permittivity, E_{F} and ε_{F} are respectively the electric field and relative background permittivity of the ferroelectric, while k is the coupling constant governing the domain wall energy and grad P denotes the gradient of P. The total polarisation in the ferroelectric is thus given by $P_{\mathrm{T}} = P + (\varepsilon_{\mathrm{F}} - 1)\varepsilon_0 E_{\mathrm{F}}$ and the electric displacement is $D = P + \varepsilon_{\mathrm{F}}\varepsilon_0 E_{\mathrm{F}}$.[20] We will assume that the ferroelectric has a second-order phase transition with $\alpha < 0$, $\beta > 0$. When we consider the ferroelectric capacitors shown in Fig. 1 the overall electrostatic energy (in Joule) consists of three contributions[21]

$$\begin{aligned}
\mathcal{U}_{\mathrm{F}} &= \frac{V_{\mathrm{T}}}{2}\int_{\mathrm{A}} \varepsilon_0 \varepsilon_{\mathrm{F}} E_{\mathrm{F,T}}(\bar{r})\mathrm{d}\bar{r},\\
\mathcal{U}_{\mathrm{B}} &= -V_{\mathrm{T}}\left[d^2 \sum_{j=1}^{n_D} P_j + \int_{\mathrm{A}} \varepsilon_0 \varepsilon_{\mathrm{F}} E_{\mathrm{F,T}}(\bar{r})\mathrm{d}\bar{r}\right],\\
\mathcal{U}_{\mathrm{D}} &= \sum_{j=1}^{n_{\mathrm{D}}} \int_{D_j} \frac{P_j V_D(\bar{r})}{2}\mathrm{d}\bar{r}
\end{aligned} \qquad (2)$$

namely the ferroelectric self-energy, $\mathcal{U}_{\mathrm{F}}$, the $\mathcal{U}_{\mathrm{B}}$ related to the external battery, and the electrostatic energy, $\mathcal{U}_{\mathrm{D}}$, due to the dielectric region, which is zero in a MFM structure. Denoted by t_{F} is the ferroelectric thickness; $E_{\mathrm{F,T}}(\bar{r}) = E_{\mathrm{F},z}(\bar{r}, -t_{\mathrm{F}})$ in eqn (2) is the electric field at the top metal interface and n_{D} is the

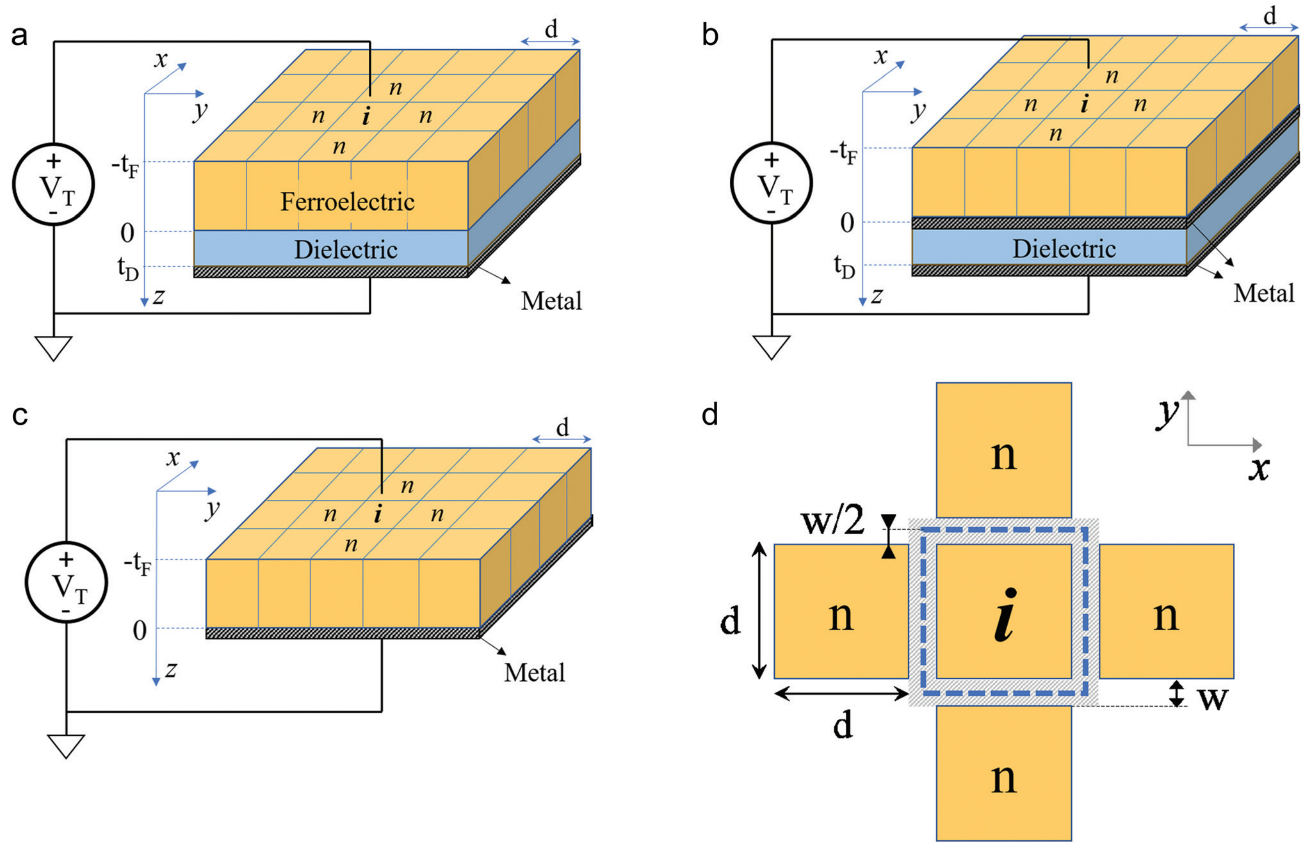

Fig. 1 Ferroelectric capacitors and related symbols. (a) Metal–Ferroelectric–Insulator–Metal (MFIM) and the reference coordinate system. (b) Metal–Ferroelectric–Metal–Insulator–Metal (MFIMIM) system. (c) Metal–Ferroelectric–Metal (MFM) structure. The top metal contact is not shown for clarity. t_{F} and t_{D} denote respectively the ferroelectric and dielectric thickness, d is the domain side of a square domain of area d^2, and V_{T} is the externally applied voltage. $V_{\mathrm{D}}(\bar{r})$ is the electrostatic potential at the oxide interface (*i.e.* at $z = 0$), that depends on $\bar{r} = (x, y)$ in a MFIM system, whereas it is independent of $\bar{r}$ in a MFMIM capacitor. (d) Sketch of the ferroelectric domain i and its nearest neighbor domains n in the x–y plane. The shaded area illustrates the domain-wall region, where w denotes the width, and the dashed blue line delimits the region used to compute the domain wall energy $u_{\mathrm{W},i}$ in eqn (4).

number of domains. When we sum $\mathcal{U}_F$, $\mathcal{U}_B$, and $\mathcal{U}_D$ and normalise to the domain area d^2 we obtain

$$U_{ET} = -\frac{V_T}{2}\frac{1}{d^2}\int_A \varepsilon_0\varepsilon_F E_{F,T}(\bar r)d\bar r - V_T\sum_{j=1}^{n_D}P_j + \frac{1}{d^2}\sum_{j=1}^{n_D}\int_{D_j}\frac{P_jV_D(\bar r)}{2}d\bar r \ [\mathrm{J\ m^{-2}}] \quad (3)$$

As for the domain wall energy, the polarisation is assumed to be essentially constant within each domain, so that grad P in eqn (1) is non null only in the domain wall region shown in Fig. 1(d). The contribution $u_{W,i}$ to the domain wall energy can thus be written as

$$u_{W,i} = \sum_n k\left(\frac{P_i - P_n}{w}\right)^2 \quad (4)$$

where w is the domain wall width shown in Fig. 1(d), which we assume to be small enough to justify the discretized form of grad P in eqn (4) and, in particular, much smaller than d. We can now integrate $u_{W,i}$ over the domain wall region inside the blue line shown in Fig. 1(d) and along t_F, and then normalise to the domain area d^2, so as to obtain the domain wall energy per unit area

$$U_W = \sum_{j=1}^{n_D}\left[\frac{t_F}{2d}\sum_n\frac{k}{w}(P_j - P_n)^2\right] \ [\mathrm{J\ m^{-2}}] \quad (5)$$

The difference between the MFM, MFIM and MFMIM systems is in the U_{ET} defined in eqn (3). In the MFM case the last term in eqn (3) is zero and $E_{F,T} = V_T/t_F$, so that $U_{ET} = -V_T\sum_{j=1}^{n_D}P_j - (n_DC_FV_T^2)/2$ with $C_F = \varepsilon_0\varepsilon_F/t_F$. For the MFMIM structure the metal interlayer results in one-dimensional electrostatics, so that $E_{F,T}$ and V_D are independent of $\bar r$ and given by $E_{F,T} = (C_DV_T - P_{AV})/(t_FC_0)$, $V_D = (C_FV_T + P_{AV})/C_0$,[18] where $P_{AV} = \left(\sum_{j=1}^{n_D}P_j\right)/n_D$ is the average polarisation, $C_D = \varepsilon_0\varepsilon_D/t_D$ (where t_D denotes the dielectric thickness) and $C_0 = (C_D + C_F)$. For the MFIM system, instead, the calculation of the ferroelectric and dielectric fields is a three-dimensional problem that demands numerical evaluation. We show in ESI section S1† that for both the MFMIM and the MFIM systems the electrostatic energy reads

$$U_{ET} = U_{dep} - V_T\frac{C_D}{C_0}\sum_j^{n_D}P_j - \frac{C_SV_T^2}{2}n_D \quad (6)$$

where $C_S = (C_FC_D)/(C_F + C_D)$. Here U_{dep} denotes the depolarisation energy defined as

$$\mathrm{MFMIM}:\ U_{dep} = \frac{n_DP_{AV}^2}{2C_0} \qquad \mathrm{MFIM}:\ U_{dep} = \frac{1}{2}\sum_{j,h=1}^{n_D}\frac{P_jP_h}{C_{j,h}} \quad (7)$$

where the capacitances $C_{j,h}$ are defined in eqn (S4) of ESI section S1,† they obey the sum rules in eqn (S7),† and all $1/C_{j,h}$ tend to zero when t_D tends to zero. As it can be seen, the depolarisation energy U_{dep} vanishes when the dielectric thickness t_D tends to zero. For all the systems shown in Fig. 1 the overall free energy is $U_T = \sum_{j=1}^{n_D}(\alpha P_j^2 + \beta P_j^4 + \gamma P_j^6) + U_W + U_{ET}$ and the corresponding dynamic equations read

$$\mathrm{MFM}:\ t_F\rho\frac{dP_i}{dt} = -\frac{\partial U_T}{\partial P_i} = \underbrace{-(2\alpha P_i + 4\beta P_i^3 + 6\gamma P_i^5)t_F - \frac{t_F}{d}\sum_n\frac{k}{w}(P_i - P_n)}_{=\partial U_{LGD}} + V_T(t) \quad (8a)$$

$$\mathrm{MFMIM}:\ t_F\rho\frac{dP_i}{dt} = \partial U_{LGD} - \frac{1}{n_DC_0}\sum_{j=1}^{n_D}P_j + \frac{C_D}{C_0}V_T(t) \quad (8b)$$

$$\mathrm{MFIM}:\ t_F\rho\frac{dP_i}{dt} = \partial U_{LGD} - \frac{1}{2}\sum_{j=1}^{n_D}\left[\frac{1}{C_{i,j}} + \frac{1}{C_{j,i}}\right]P_j + \frac{C_D}{C_0}V_T(t) \quad (8c)$$

where ρ is the resistivity governing the ferroelectric domain dynamics. It is straightforward to verify that, when the dielectric thickness t_D tends to zero, $1/C_0$ and $1/C_{i,j}$ tend to zero while $[C_D/C_0]$ tends to one, so that eqn (8b) and (8c) simplify to eqn (8a). Moreover for $n_D = 1$ eqn (8b) and (8c) are identical; in fact the MFMIM and MFIM systems are equivalent, the domain wall energy is zero and eqn (8b) and (8c) simplify to the well-known single domain equation.[18]

3. Conditions for stable NC operation

Throughout this paper we employ a definition of NC operation consisting of the polarization P_i of all domains being zero at zero external voltage V_T, which ensures a hysteresis-free behavior also in the multi-domain picture. If the ferroelectric is stabilized in a region where P_i is not zero for most domains but $\partial^2G(P_i)/\partial^2P_i$ is negative (with $G(P_i) = (\alpha_iP_i^2 + \beta_iP_i^4 + \gamma_iP_i^6)$, an NC operation can still be claimed, albeit in the presence of hysteresis. The stable NC operation can be evaluated by inspecting the eigenvalues of the Jacobian matrices,‡ J, of the dynamic systems in eqn. (8a)–(8c) evaluated for $P_i = 0$ in all domains. Here it should be noticed that analysing the stability of the equilibrium at $P_i = 0$ and $V_T = 0$ is not restrictive. In fact, as we show in ESI section S4,† stability in this case implies stability of the equilibrium for any other constant value of V_T. The Jacobian matrices read

$$\mathbf{J}_{MFM} = \frac{1}{\rho t_F}\left[-2\alpha t_F\mathbf{I} - \frac{t_Fk}{dw}\mathbf{L}\right] \quad (9a)$$

‡ The Jacobian matrix of the system of dynamic equations $dP_i/dt = f_i(P_1,\cdots P_{nD})$ is defined component-wise as $J(i,j) = \partial f_i/\partial P_j$.

$$\mathbf{J}_{\mathrm{MFMIM}} = \frac{1}{\rho t_{\mathrm{F}}}\left[-2\alpha t_{\mathrm{F}}\mathbf{I} - \frac{t_{\mathrm{F}}k}{dw}\mathbf{L} - \frac{\mathbf{O}_{\mathrm{dep}}}{n_{\mathrm{D}}C_0}\right] \tag{9b}$$

$$\mathbf{J}_{\mathrm{MFIM}} = \frac{1}{\rho t_{\mathrm{F}}}\left[-2\alpha t_{\mathrm{F}}\mathbf{I} - \frac{t_{\mathrm{F}}k}{dw}\mathbf{L} - \mathbf{C}_{\mathrm{dep}}\right] \tag{9c}$$

where $\mathbf{I}$ is the n_{D} by n_{D} identity matrix, while $\mathbf{L}$ is the Laplacian matrix.§ The matrix $\mathbf{O}_{\mathrm{dep}}$ has all entries equal to one, whereas $\mathbf{C}_{\mathrm{dep}}$ is defined as

$$C_{\mathrm{dep}}(i,j) = \frac{1}{2}\left[\frac{1}{C_{i,j}} + \frac{1}{C_{j,i}}\right] \tag{10}$$

The matrices $\mathbf{O}_{\mathrm{dep}}$ and $\mathbf{C}_{\mathrm{dep}}$ stem from the depolarisation energy U_{dep} in eqn (7), and are very different for a MFMIM and a MFIM system. The eigenvalues of the symmetric J matrices in eqn (9) are real valued and, for a stable NC operation, it is required that the largest eigenvalue $\sigma_{\max}(J)$ of the Jacobian matrix evaluated for all $P_i = 0$ be negative.[22] This results in the equivalent stability conditions

$$\mathrm{MFM}: \frac{k}{dw}\sigma_{\min}(\mathbf{L}) > 2|\alpha| \tag{11a}$$

$$\mathrm{MFMIM}: \sigma_{\min}\left[\frac{t_{\mathrm{F}}k}{dw}\mathbf{L} + \frac{\mathbf{O}_{\mathrm{dep}}}{n_{\mathrm{D}}C_0}\right] > 2|\alpha|t_{\mathrm{F}} \tag{11b}$$

$$\mathrm{MFIM}: \sigma_{\min}\left[\frac{t_{\mathrm{F}}k}{dw}\mathbf{L} + \mathbf{C}_{\mathrm{dep}}\right] > 2|\alpha|t_{\mathrm{F}} \tag{11c}$$

where $\sigma_{\min}(\mathbf{M})$ denotes the smallest eigenvalue of the matrix $\mathbf{M}$.

We now recall that the eigenvalues of $\mathbf{L}$ are known analytically in our case (since we are dealing with a rectangular grid) and the smallest and second smallest eigenvalues are $\sigma_0(\mathbf{L}) = 0$ and $\sigma_1(\mathbf{L}) = \left[2\sin\left(\pi/\left(2\sqrt{n_{\mathrm{D}}}\right)\right)\right]^2$.[23] This implies that, as expected, the MFM system is always unstable for all $P_i = 0$.

For the MFMIM system we show in ESI section S2† that, due to the peculiar form of the matrix $\mathbf{O}_{\mathrm{dep}}$, one can derive the analytical (necessary and sufficient) condition for a stable NC operation given by

$$\min\left\{\frac{1}{C_0}, \frac{t_{\mathrm{F}}k}{dw}\left[2\sin\left(\pi/\left(2\sqrt{n_{\mathrm{D}}}\right)\right)\right]^2\right\} > 2|\alpha|t_{\mathrm{F}} \tag{12}$$

Eqn (12) shows that in the MFMIM system the effect of the depolarisation energy is very limited; in fact $\mathbf{O}_{\mathrm{dep}}$ can only eliminate the influence of $\sigma_0(\mathbf{L}) = 0$ but not the influence of $\sigma_1(\mathbf{L})$. Eqn (12) also affirms that the condition $(1/C_0) > 2|\alpha|t_{\mathrm{F}}$ is necessary for the stability of the MFMIM system. Moreover, for a relatively large number of domains such that $\sin\left(\pi/\left(2\sqrt{n_{\mathrm{D}}}\right)\right) \simeq \pi/\left(2\sqrt{n_{\mathrm{D}}}\right)$, eqn (12) suggests that a stable NC operation for the MFMIM system requires k/w values that increase proportionally to n_{D}, hence to the device area.

For the MFIM structure it is not possible to derive analytical eigenvalues and stability conditions from eqn (11c), but numerical analysis shows that $\mathbf{C}_{\mathrm{dep}}$ has a much larger influence on NC stabilisation than $\mathbf{O}_{\mathrm{dep}}$ has for the MFMIM system. Moreover we show in ESI section S3† that even for the MFIM system the inequality $(1/C_0) > 2|\alpha|t_{\mathrm{F}}$ is still a necessary condition for a stable NC operation. It is interesting to note that this is the stability condition previously derived for a single domain system.[18]

Ferroelectric materials may have domain to domain statistical variations of the ferroelectric anisotropy constants, whose influence on stable NC operation is addressed in ESI section S5.†

§ $\mathbf{L}$ is defined component-wise as $\mathbf{L}(i,j) = -1$ if domain j is a neighbour of domain i and $\mathbf{L}(i,j) = 0$ otherwise (see Fig. 1(d)), and $\mathbf{L}(i,i) = -\sum_{j\neq i}\mathbf{L}(i,j)$.

4. Physical insight and design space

All the simulation results reported in this work were obtained for $\varepsilon_{\mathrm{F}} = 33$, $\varepsilon_{\mathrm{D}} = 23.5$, $t_{\mathrm{F}} = 11.6$ nm, $t_{\mathrm{D}} = 13.5$ nm, $\alpha = -4.6 \times 10^8$ m F^{-1}, $\beta = 9.8 \times 10^9$ m^5 C^{-2} F^{-1} and $\gamma = 0$, if not otherwise stated, namely the material parameters that have been reported for the $Hf_{0.5}Zr_{0.5}O_2$–Ta_2O_5 MFIM system in ref. 13.

Fig. 2(a) shows the maximum eigenvalue $\sigma_{\max}$ of the Jacobian for all $P_i = 0$ *versus* the coupling factor k for either MFMIM or MFIM structures with an area $A = 2500$ nm^2, and for different combinations of n_{D} and d. As it can be seen the MFIM capacitor can achieve NC stabilisation for smaller k values compared to the MFMIM system, and it has a much weaker sensitivity to the increase of n_{D}. The substantial difference in the NC stabilisation of MFMIM and MFIM systems for a large n_{D} is better illustrated in Fig. 2(b), showing that for the MFMIM system the k value required for NC stabilisation increases proportionally to n_{D} and thus to the device areas. This makes NC stabilisation practically impossible for MFMIM systems having areas as those used in recent experiments.[14–16]

Fig. 2(c) and (d) focus on the MFIM system and show respectively the numerically calculated $\sigma_{\max}$ of the Jacobian matrix (for all $P_i = 0$) for different t_{D} and at fixed t_{F}, and the design regions for a stable NC operation of a MFIM structure in the t_{D}–k plane and for $n_{\mathrm{D}} = 100$. As it can be seen the NC operation is not possible for very thin oxides, because the necessary condition $(1/C_0) > 2|\alpha|t_{\mathrm{F}}$ is not fulfilled and, for any t_{D} satisfying the above condition, we have a minimum k value necessary for stabilisation. For t_{D} larger than about 10 nm the k for NC stabilisation becomes independent of t_{D}. This occurs because at small t_{D} the potential V_{D} at the ferroelectric–dielectric interface and the depolarisation energy U_{dep} decrease by scaling t_{D} and at large t_{D} the U_{dep} becomes insensitive to t_{D}.

According to the empirical formula for NC stable operation of a one-dimensional and periodic MFIM system proposed in eqn (15) of ref. 18, the t_{D} independent k value necessary for NC operation is $k = 1.2 \times 10^{-9}$ [m^3 F^{-1}] for $t_{\mathrm{F}} = 11.6$ nm, and $k = 2.1 \times 10^{-9}$ [m^3 F^{-1}] for $t_{\mathrm{F}} = 20$ nm. These k values are about two times larger than the values in Fig. 2(d) obtained for the two-dimensional ferroelectric domain arrangement studied in this work. In more general terms we found that, while the qualitative trends obtained from our 3D analysis are similar to those predicted using eqn (15) of ref. 18, the regions for NC stabilization identified by our results are larger. For example our 3D

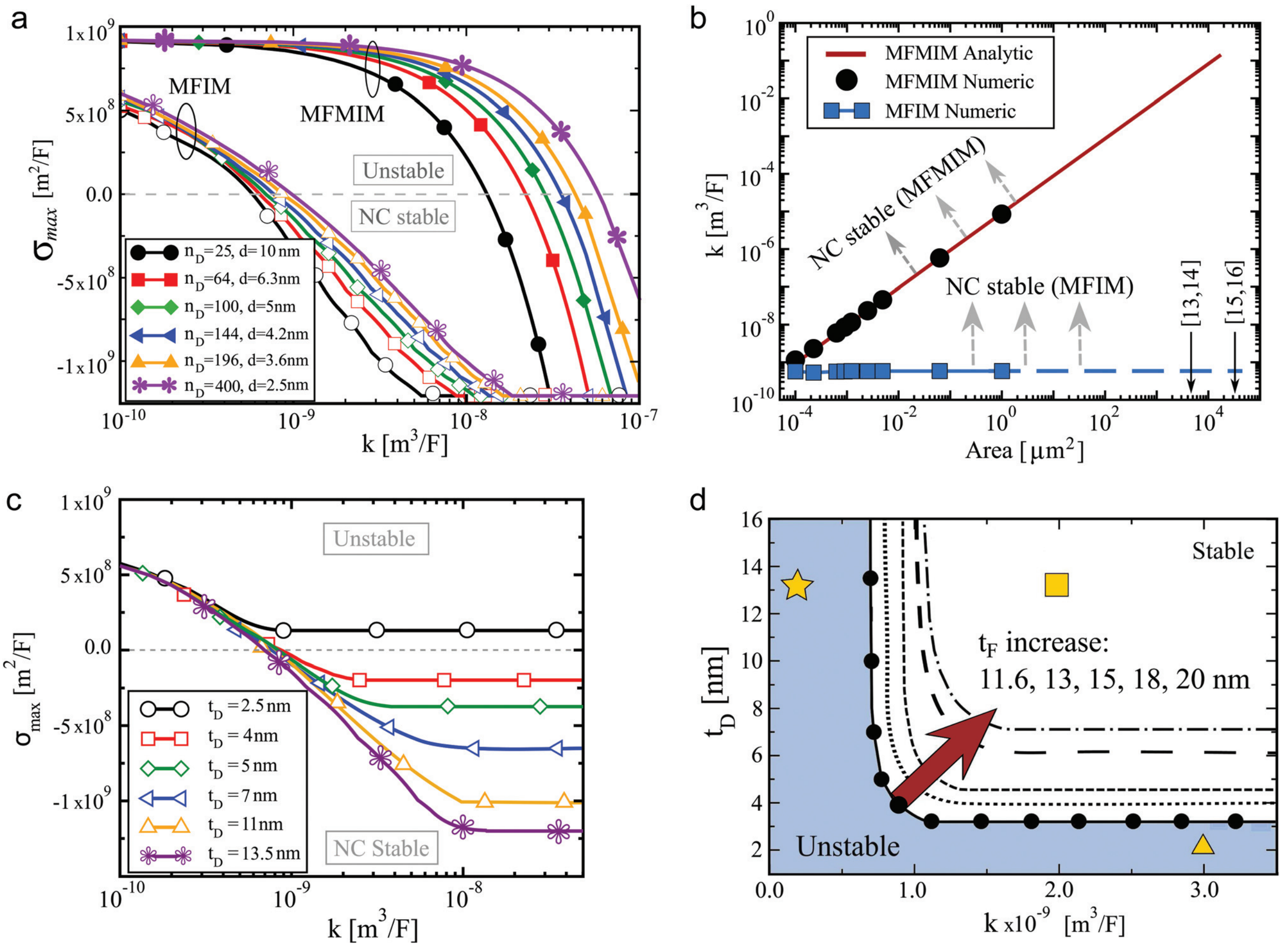

Fig. 2 Eigenvalues of the Jacobian matrix and design space for stable NC operation: (a) largest eigenvalue σ_{max} of the Jacobian matrix for all $P_i = 0$ *versus* the domain wall coupling factor k for either a MFIM (numerically calculated) or a MFMIM structure. Capacitor area is A = 2500 nm^2 and the results are shown for different combinations of d and n_D. Stable NC operation corresponds to $\sigma_{max} < 0$. (b) Minimum coupling factor k necessary for a stable NC operation *versus* the capacitor area for either a MFMIM or a MFIM structure. For the MFIM structure results have been calculated numerically from the condition $\sigma_{max} < 0$, while for the MFMIM structure results stem from eqn (12). Domain size is d = 5 nm, thus Area = $d^2 n_D$. Please note the large areas corresponding to recent experiments in ref. 13–16. (c) Maximum eigenvalue σ *versus* coupling factor k obtained from numerical simulations for a MFIM structure having different Ta_2O_5 thicknesses t_D. Ferroelectric thickness, domain number n_D and domain area d^2 set to t_F = 11.6 nm, n_D = 100 and d^2 = 25 nm^2. (d) Regions for stable NC operation for a MFIM structure in the t_D *versus* k plane and for different t_F values. Filled circles correspond to t_F = 11.6 nm. For larger t_F values the minimum t_D required for stability increases, as predicted by the necessary condition $(1/C_0) > 2|\alpha|t_F$. Area is A = 2500 nm^2 and n_D = 100. The star, square and triangle symbols identify the t_D and k values corresponding to some of the simulations in Fig. 3, and are discussed in the text.

results suggest that, for a given couple (t_D, t_F), a smaller k is sufficient for stabilization and, for a given (t_D, k), the system is NC stable up to larger t_F values.

While Fig. 2 illustrates the design space for a stable NC operation, it is also insightful to inspect the steady-state configuration of domains obtained by solving the LGD dynamic equations. In this respect, Fig. 3(a) shows the steady-state domain configuration at V_T = 0 for a MFIM system corresponding to the triangle symbol in Fig. 2(d), namely to a system where the condition $(1/C_0) > 2|\alpha|t_F$ necessary for NC stabilisation is not fulfilled. As it can be seen the MFIM evolves so as to minimise the domain wall energy, whose minimum value is achieved by having all the domains with a positive polarisation. This steady-state polarisation pattern resembles the pattern of a MFM system, which the MFIM capacitor in fact approximates when t_D and U_{dep} become very small. Fig. 3(b), instead, illustrates the case corresponding to the star symbol in Fig. 2(d), namely to a system where the condition $(1/C_0) > 2|\alpha|t_F$ is fulfilled, but the domain wall constant k is too small for the NC stabilisation. In this case the system tends to minimise the depolarisation energy by having domains with different polarisations, even if this implies a larger domain wall energy compared to the pattern in Fig. 3(a). Fig. 3(c) and (d) illustrate the steady-state domain configuration at V_T = 0 for a MFIM with $k = 2 \times 10^{-9}$ m^3 F^{-1} (square symbol in Fig. 2(d)), and for the counterpart MFMIM. Consistent with Fig. 2(d), the steady-state condition for the MFIM system corresponds to all P_i = 0. The MFMIM, instead, is not stable

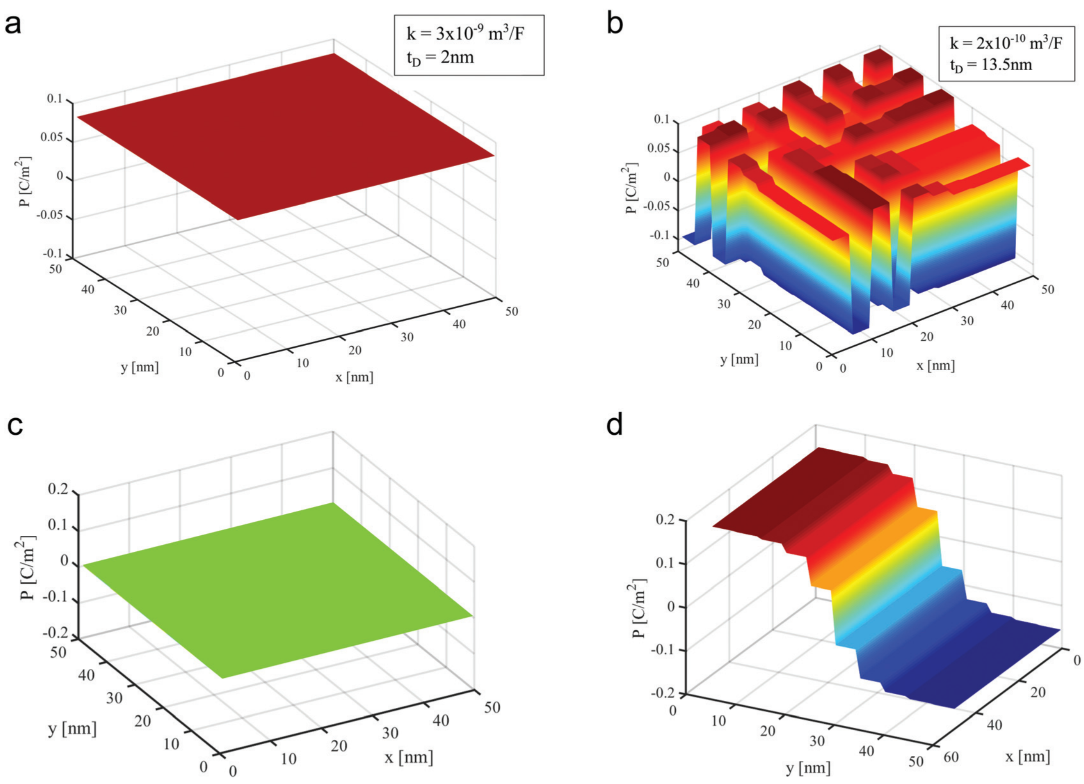

Fig. 3 Ferroelectric domain patterns for MFIM and MFMIM capacitors. Steady-state domain configuration at V_T = 0 V. (a) MFIM system: small t_D and high k value that do not correspond to a stable NC operation, see triangle in Fig. 2(b). (b) MFIM system: large t_D and small k value that do not correspond to a stable NC operation, see star in Fig. 2(b). (c) MFIM system with t_D = 13.5 nm, t_F = 11.6 nm and $k = 2 \times 10^{-9}$ m^3 F^{-1}, which correspond to a stable NC operation, see square in Fig. 2(b). (d) MFMIM capacitor having the same material and device parameters as the MFIM in (c).

for all P_i = 0, and therefore it evolves to a configuration corresponding to $P_{AV} = \left(\sum_{i=1}^{n_D} P_i\right)/n_D \simeq 0$.

Fig. 3(c) and (d) show that the crucial difference between MFMIM and MFIM systems is that the depolarisation energy of the MFMIM system at V_T = 0 is zero if P_{AV} is zero (see eqn (7)). Hence if the MFMIM is initialised with all P_i = 0, it gets destabilised along trajectories having $P_{AV} \simeq 0$ and thus $U_{dep} \simeq 0$, which is confirmed by the steady-state configuration shown in Fig. 3(d). The same trajectories are precluded in the MFIM system because the corresponding U_{dep} in eqn (7) is not at all zero, hence it is the form of the U_{dep} which makes the NC stabilisation possible in MFIM capacitors.

The analysis developed in this paper and the results presented in this section were performed and obtained under the assumption that the leakage current through the oxides is small enough to not influence the NC stabilization. As already recognized in ref. 24 and 25, in a MFMIM structure the presence of a non negligible leakage essentially precludes the NC stabilization.

5. Comparison with experimental results

As a validation of our modelling approach we now illustrate a systematic comparison with recent experiments reported for an $Hf_{0.5}Zr_{0.5}O_2$ based MFIM structure.[12,13] The simulations account for the presence of a fixed charge Q_{DF} = 0.15 C cm^{-2} at the interface between $Hf_{0.5}Zr_{0.5}O_2$ and Ta_2O_5, which results in the fact that the ferroelectric is biased in the negative polarisation branch for V_T = 0 V.[12] Simulations correspond to a domain size of d = 5 nm and a domain number n_D = 100, and we verified that the results are insensitive to any further n_D increase. The pulse width of the trapezoidal input waveform $V_T(t)$ is set to 1 μs (if not otherwise stated), which is small enough to make the ferroelectric time constants practically negligible for the small resistivity value ρ = 0.5 mΩ m employed in these simulations.

Fig. 4(a) shows the charge $Q = P + \varepsilon_F\varepsilon_0 E_F + Q_{DF}$ *versus* the top value V_{max} of the trapezoidal voltage waveform applied across the $Hf_{0.5}Zr_{0.5}O_2$–Ta_2O_5 capacitor, and shows a good agreement between simulations and experiments. Fig. 4(b) illustrates the simulated waveforms for the ferroelectric field, E_F, and the total ferroelectric polarization, $P_T = P + \varepsilon_F\varepsilon_0 E_F$, produced by trapezoidal input V_T and for three V_T amplitudes. By using the E_F and P_T values observed in Fig. 4(b), we obtained the charge *versus* ferroelectric field curves reported in Fig. 4(c) and (d) respectively for the $Hf_{0.5}Zr_{0.5}O_2$–Ta_2O_5 and $Hf_{0.5}Zr_{0.5}O_2$–Al_2O_3 capacitors. As it can be seen simulations nicely reproduce the fact that, for the experimental conditions under study, the ferroelectric layer can be operated in the NC operation region, which is the physical origin of the change of

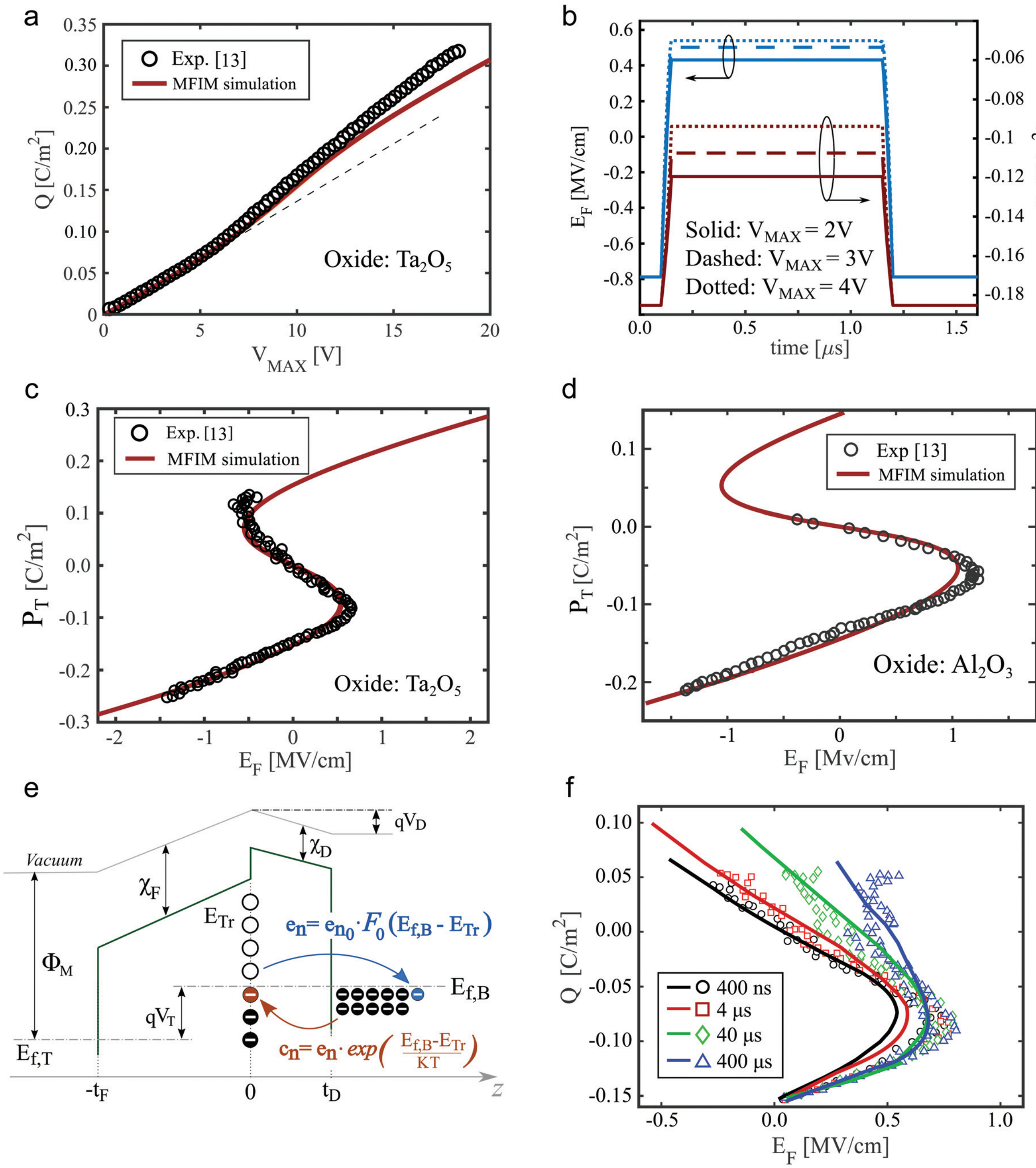

Fig. 4 Comparison between simulations and experiments. Measurements (symbols) and simulations (lines) for the MFIM structures in ref. 12 and 13. For the $Hf_{0.5}Zr_{0.5}O_2$–Ta_2O_5 capacitor the simulation parameters are ε_F = 33, ε_D = 23.48, t_F = 11.6 nm, t_D = 13.5 nm, $\alpha = -4.6 \times 10^8$ m F^{-1}, and $\beta = 9.8 \times 10^9$ m^5 C^{-2} F^{-1}, while for the $Hf_{0.5}Zr_{0.5}O_2$–Al_2O_3 system the parameters are ε_D = 8, t_F = 7.7 nm, t_D = 4 nm, $\alpha = -9.45 \times 10^8$ m F^{-1} and $\beta = 4.5 \times 10^9$ m^5 C^{-2} F^{-1};[12,13] for both capacitors we used ρ = 0.5 mΩ m and $k = 2 \times 10^{-9}$ m^3 F^{-1} m^{-1}. (a) Reversibly stored and released charge, Q, *versus* the top value V_{MAX} of the trapezoidal voltage waveform across the capacitor. (b) Simulated ferroelectric field and charge *versus* time produced by a trapezoidal input V_T with a pulse width of 1 µs and for different V_T amplitudes. (c) Polarisation *versus* ferroelectric electric field for the $Hf_{0.5}Zr_{0.5}O_2$–Ta_2O_5 MFIM capacitor. (d) Polarisation *versus* ferroelectric electric field for the $Hf_{0.5}Zr_{0.5}O_2$–Al_2O_3 capacitor. (e) Sketch of the band structure of the MFIM device with representation of the emission and capture mechanisms. (f) Simulated charge *versus* ferroelectric E_F curves for different pulse widths of the input signal and fixed density $N_T = 7.5^{12}$ eV^{-1} cm^{-2} of acceptor type interface traps with a uniform energy distribution. In these simulations the emission rate is $e_{n0} = 5 \times 10^4$ s^{-1}, the metal gate work-function is Φ_M = 4.05 eV, and the electron affinity is χ_F = 2.2 eV for $Hf_{0.5}Zr_{0.5}O_2$ and χ_D = 3.2 eV for Ta_2O_5.[29]

slope in the Q *versus* V_{max} plot of Fig. 4(b). We also verified that, as long as the NC stabilization is guaranteed, different t_D values still result in the same P_T *versus* E_F curves for the quasi-static NC operation explored in this work.

From the charge *versus* V_T plots as in Fig. 4(a) we numerically calculated the capacitance $C_T = (\partial Q/\partial V_T)$ in the NC stabilized region and compared to the results of the simple analytical expression $C_T = C_D \cdot [|C_{F,0}|/(|C_{F,0}| - C_D)]$, with $C_{F,0} = [1/2\alpha t_F +$

ε_F/t_F] being the zero field ferroelectric capacitance. This analysis showed that, while the numerically calculated C_T is quite bias dependent even inside the NC region, the analytical expression is in very close agreement with the maximum C_T. Because the term $[|C_{F,0}|/(|C_{F,0}| - C_D)]$ can be seen as an enhancement factor of C_T with respect to C_D, the analytical expression allows one to easily estimate the capacitance enhancement from the dielectric and ferroelectric parameters ε_D, t_D, α, ε_F, and t_F.

We also developed a model to study the influence of traps at the ferroelectric–dielectric interface, according to a simple kinetic equation for the trap occupation that we solved self-consistently with the LGD equations, as discussed in detail in the ESI section S6.† Fig. 4(e) illustrates that traps are assumed to exchange electrons *via* tunneling with the bottom metal contact. While the bias independent rate e_{n0} could be described by models similar to those used for border traps in MOS transistors,[26,27] such a quantitative description of the emission rates goes beyond the scope of the present work, where we investigate only the qualitative features induced by traps and, to this purpose, we consider e_{n0} as a free parameter in the comparison to experiments. In this respect, Fig. 4(f) illustrates experiments and simulations for the charge *versus* ferroelectric field obtained for different pulse widths of the trapezoidal input waveform, where simulations correspond to a uniform density $N_T = 7.5 \times 10^{12}$ eV^{-1} cm^{-2} of acceptor type traps. As it can be seen, by using $e_{n0} = 5.0 \times 10^4$ s^{-1} the simulations can reproduce quite well the influence of the pulse width on the Q *versus* E_F curves observed in experiments. The influence of traps on the stability conditions of a MFIM system is further addressed in ESI section S6.†

In summary, we present a methodology to investigate a possible stable NC operation in ferroelectric capacitors based on the LGD dynamic equations duly accounting for the three-dimensional nature of the problem. From the Jacobian matrix of the LGD equations we derived analytical or semi-analytical stability conditions that clarified important differences between a MFIM and a MFMIM system. Our analysis is consistent with the fact that a stable NC operation has been observed in MFIM systems but not in MFMIM systems, and suggests that MFMIM capacitors or capacitors externally connected to a MOSFET are inherently unsuitable to study the stable NC operation.

A systematic comparison with recent experiments in MFIM capacitors provides convincing evidence that the NC operation of the ferroelectric $Hf_{0.5}Zr_{0.5}O_2$ can nicely explain the experimental data. The critical role of interface traps emphasizes the importance of the quality of the ferroelectric–dielectric interface in the NC operation of ferroelectric capacitors and transistors.

We conclude by remarking that, while in a robustly NC stabilized system domains tend to move together thus resulting in fairly 1D electrostatics, we verified that the electrostatics becomes strongly 3D when domain nucleation occurs and the system becomes hysteretic. The methodology for the dynamics of the ferroelectric domain developed in this paper is thus expected to be important also for the analysis of a transient and possibly hysteretic NC operation, as well as for the investigation of ferroelectric tunnelling junctions to be used either as non volatile memories or as memristors for neuromorphic computing applications.[28]

Conflicts of interest

There are no conflicts to declare.

References

1 S. Salahuddin and S. Datta, Use of Negative Capacitance to Provide Voltage Amplification for Low Power Nanoscale Devices, *Nano Lett.*, 2008, **8**(2), 405–410, DOI: 10.1021/nl071804g.

2 A. I. Khan, On the Microscopic Origin of Negative Capacitance in Ferroelectric Materials: A Toy Model, in *2018 IEEE International Electron Devices Meeting (IEDM)*, 2018, pp. 9.3.1–9.3.4, DOI: 10.1109/IEDM.2018.8614574, ISSN 2156-017X.

3 J. C. Wong and S. Salahuddin, Negative Capacitance Transistors, *Proc. IEEE*, 2019, **107**(1), 49–62.

4 T. N. Theis and P. M. Solomon, In Quest of the Next Switch: Prospects for Greatly Reduced Power Dissipation in a Successor to the Silicon Field-Effect Transistor, *Proc. IEEE*, 2010, **98**(12), 2005–2014.

5 A. C. Seabaugh and Q. Zhang, Low-Voltage Tunnel Transistors for Beyond CMOS Logic, *Proc. IEEE*, 2010, **98**(12), 2095–2110, DOI: 10.1109/JPROC.2010.2070470.

6 Z. Krivokapic, U. Rana, R. Galatage, A. Razavieh, A. Aziz, J. Liu, J. Shi, H. Kim, R. Sporer, C. Serrao, A. Busquet, P. Polakowski, J. Mülle, W. Kleemeier, A. Jacob, D. Brown, A. Knorr, R. Carter and S. Banna, GLOBALFOUNDRIES, "14 nm Ferroelectric FinFET Technology with Steep Subthreshold Slope for Ultra Low Power Applications, in *2017 IEEE International Electron Devices Meeting (IEDM)*, 2017, pp. 357–360, DOI: 10.1109/IEDM.2017.8268393. ISSN 2156-017X.

7 D. Kwon, Y. Liao, Y. Lin, J. P. Duarte, K. Chatterjee, A. J. Tan, A. K. Yadav, C. Hu, Z. Krivokapic and S. Salahuddin, Response Speed of Negative Capacitance FinFETs, in *2018 IEEE Symposium on VLSI Technology*, 2018, pp. 49–50, DOI: 10.1109/VLSIT.2018.8510626. ISSN 2158-9682.

8 T. Rollo and D. Esseni, Energy Minimization and Kirchhoff's Laws in Negative Capacitance Ferroelectric Capacitors and MOSFETs, *IEEE Electron Device Lett.*, 2017, **38**(6), 814–817, DOI: 10.1109/LED.2017.2691002.

9 T. Rollo and D. Esseni, New Design Perspective for Ferroelectric NC-FETs, *IEEE Electron Device Lett.*, 2018, **39**(4), 603–606, DOI: 10.1109/LED.2018.2795026.

10 T. Rollo and D. Esseni, Influence of Interface Traps on Ferroelectric NC-FETs, *IEEE Electron Device Lett.*, 2018, **39**(7), 1100–1103, DOI: 10.1109/LED.2018.2842087.
11 M. A. Alam, M. Si and P. D. Ye, A critical review of recent progress on negative capacitance field-effect transistors, *Appl. Phys. Lett.*, 2019, **114**(9), 090401, DOI: 10.1063/1.5092684.
12 M. Hoffmann, B. Max, T. Mittmann, U. Schroeder, S. Slesazeck and T. Mikolajick, Demonstration of High-speed Hysteresis-free Negative Capacitance in Ferroelectric $Hf_{0.5}Zr_{0.5}O_2$, in *2018 IEEE International Electron Devices Meeting (IEDM)*, 2018, pp. 31.6.1–31.6.4, DOI: 10.1109/IEDM.2018.8614677. ISSN 2156-017X.
13 M. Hoffmann, F. P. G. Fengler, M. Herzig, T. Mittmann, B. Max, U. Schroeder, R. Negrea, P. Lucian, S. Slesazeck and T. Mikolajick, Unveiling the double-well energy landscape in a ferroelectric layer, *Nature*, 2019, **565**, 464–467, DOI: 10.1038/s41586-018-0854-z.
14 Z. Liu, M. A. Bhuiyan and T. P. Ma, A Critical Examination of 'Quasi-Static Negative Capacitance' (QSNC) theory, *2018 IEEE International Electron Devices Meeting (IEDM)*, 2018, pp. 31.2.1–31.2.4, DOI: 10.1109/IEDM.2018.8614614. ISSN 2156-017X.
15 X. Li and A. Toriumi, Direct relationship between sub-60 mV/dec subthreshold swing and internal potential instability in MOSFET externally connected to ferroelectric capacitor, in *2018 IEEE International Electron Devices Meeting (IEDM)*, 2018, pp. 31.3.1–31.3.4. ISSN 2156-017X.
16 H. Wang, M. Yang, Q. Huang, K. Zhu, Y. Zhao, Z. Liang, C. Chen, Z. Wang, Y. Zhong, X. Zhang and R. Huang, New Insights into the Physical Origin of Negative Capacitance and Hysteresis in NCFETs, *2018 IEEE International Electron Devices Meeting (IEDM)*, 2018, pp. 31.1.1–31.1.4, DOI: 10.1109/IEDM.2018.8614504. ISSN 2156-017X.
17 J. Van Houdt and P. Roussel, Physical Model for the Steep Subthreshold Slope in Ferroelectric FETs, *IEEE Electron Device Lett.*, 2018, **39**(6), 877–880, DOI: 10.1109/LED.2018.2829604.
18 M. Hoffmann, M. Pešić, S. Slesazeck, U. Schroeder and T. Mikolajick, On the stabilization of ferroelectric negative capacitance in nanoscale devices, *Nanoscale*, 2018, **10**(6), 10891–10899, DOI: 10.1039/C8NR02752H.
19 T. Rollo, F. Blanchini, G. Giordano, R. Specogna and D. Esseni, Revised analysis of negative capacitance in ferroelectric-insulator capacitors: analytical and numerical results, physical insight, comparison to experiments, in *2019 IEEE International Electron Devices Meeting (IEDM)*, 2019, pp. 7.2.1–7.2.4.
20 C. H. Woo and Y. Zheng, Depolarization in modeling nanoscale ferroelectrics using the Landau free energy functional, *Appl. Phys. A*, 2008, 59–63, DOI: 10.1007/s00339-007-4355-4.
21 E. M. Purcell, *Electricity and Magnetism*, Oxford University, 2013. ISBN 0-89871-465-6.
22 D. G. Luenberger, *Introduction To Dynamic Systems*, John Wiley & Sons, 1979. ISBN 10:0471025941.
23 M. Fiedler, Algebraic connectivity of graphs, *Czechoslovak Math. J.*, 1973, **23**(2), 298–305. Available Online: http://eudml.org/doc/12723.
24 A. I. Khan, U. Radhakrishna, S. Salahuddin and D. Antoniadis, Work Function Engineering for Performance Improvement in Leaky Negative Capacitance FETs, *IEEE Electron Device Lett.*, 2017, **38**(9), 1335–1338, DOI: 10.1109/LED.2017.2733382.
25 A. I. Khan, U. Radhakrishna, K. Chatterjee, S. Salahuddin and D. A. Antoniadis, Negative Capacitance Behavior in a Leaky Ferroelectric, *IEEE Trans. Electron Devices*, 2016, **63**(11), 4416–4422.
26 A. Palma, A. Godoy, J. A. Jiménez-Tejada, J. E. Carceller and J. A. López-Villanueva, Quantum two-dimensional calculation of time constants of random telegraph signals in metal-oxide–semiconductor structures, *Phys. Rev. B: Condens. Matter Mater. Phys.*, 1997, **56**, 9565–9574, DOI: 10.1103/PhysRevB.56.9565.
27 F. Jiménez-Molinos, F. Gámiz, A. Palma, P. Cartujo and J. A. López-Villanueva, Direct and trap-assisted elastic tunneling through ultrathin gate oxides, *J. Appl. Phys.*, 2002, **91**(8), 5116–5124, DOI: 10.1063/1.1461062.
28 B. Sören, G. Julie, L. Gwendal, X. Bin, L. Nicolas, F. Stéphane, G. Stéphanie, C. Cécile, G. Karin, X. Stéphane, T. Jean, B. Laurent, B. Manuel, B. Agnès, S. Sylvain and G. Vincent, Learning through ferroelectric domain dynamics in solid-state synapses, *Nat. Commun.*, 2017, **8**, 14736, DOI: 10.1038/ncomms14736.
29 B. C. Lai and J. Y.-m. Lee, Leakage Current Mechanism of Metal-Ta_2O_5-Metal Capacitors for Memory Device Applications, *J. Electrochem. Soc.*, 1999, **146**, 266, DOI: 10.1149/1.1391597.